JOURNAL OF PROPULSION AND POWER
Vol. 26, No. 5, September–October 2010

Investigation of a Fluidic Shock Control Method for Hypersonic Inlets

Hui-Jun Tan,* Cheng-Hong Li,† and Yue Zhang†
Nanjing University of Aeronautics and Astronautics, 210016 Nanjing, People's Republic of China

DOI: 10.2514/1.48513

To realize the control of the ramp shock system of hypersonic inlets, the current study involves a fluidic shock control technique featured by fixed geometry. First, a theoretical analysis and design method for this technique is developed, including the calculation of the shock control requirement of a typical hypersonic variable inlet, the analysis of the shock control capability of a set of S-shaped surfaces attached to a ramp surface, the estimation of the required secondary-to-primary mass flow ratio, and the realization of an aerodynamic curved surface by distributed air injections. Then, the correctness of the method and the underlying flow mechanism are verified by computational fluid dynamics with a two-dimensional case. Finally, a three-dimensional test model is designed and investigated by experiments and computations to demonstrate the capability of the fluidic shock control technique, examine the three-dimensional effects, and verify the computational fluid dynamics tool. The results show that the shock control capability of this technique can meet the requirement of hypersonic variable inlets operating from Mach 4 to 6. At a secondary-to-primary mass flow ratio of 1% or less, the first ramp shock can be consistently maintained on the cowl lip from Mach 5 to 6.

Nomenclature

H	=	shape factor of the boundary layer
h_{cap}	=	theoretical capture height
h_{disp1}	=	maximum displacement of the first shock
h_{disp2}	=	maximum displacement of the second shock
h_{en}	=	height of the duct entrance
h_{th}	=	height of the throat
h_1	=	passage height of the primary flow after the first shock
L_{curved}	=	length of the attached curved surface
L_{fore}	=	length of the forebody
L_{start}	=	start position of the attached curved surface
M_{max}	=	maximum Mach number
M_s	=	average Mach number of the secondary flow, directly downstream of the injection region
M_{sh}	=	shock-on-lip Mach number
M_0	=	freestream Mach number
M_1	=	average Mach number of the primary flow after the first ramp shock
$\dot{m}_p$	=	mass flow rate of the primary flow
$\dot{m}_s$	=	mass flow rate of the secondary flow
p_s	=	average static pressure of the secondary flow, directly downstream of the injection region
p_1	=	average static pressure of the primary flow after the first ramp shock
p_c^*	=	total pressure of the secondary flow in the supply chamber
Q	=	mass flow coefficient of the multislot plate
T_s	=	average static temperature of the secondary flow, directly downstream of the injection region
T_1	=	average static temperature of the primary flow after the first ramp shock
W_{offset}	=	height of the attached curved surface
W_{slot}	=	total width of the injection slots
α_1	=	first ramp angle
α_2	=	second ramp angle
β_1	=	first ramp shock angle
β_2	=	second ramp shock angle
Δ	=	slot width
δ	=	nominal thickness of the boundary layer
δ^*	=	displacement thickness of the boundary layer
θ	=	momentum thickness of the boundary layer
σ	=	total pressure ratio of the ramp shock

Received 11 December 2009; revision received 20 May 2010; accepted for publication 20 May 2010.

*Professor, College of Energy and Power Engineering.
†Graduate Student, College of Energy and Power Engineering.

I. Introduction

A HYPERSONIC inlet is one of the three critical aerodynamic components of a scramjet. The overall performance of a scramjet, and even the vehicles, is largely dictated by the aerodynamic performance, geometric size, and weight of the hypersonic inlets [1]. Commonly, hypersonic inlets have a wide Mach number range, but the shock-on-lip (SOL) condition can be met only at the design Mach number, since shock angles vary with the upstream Mach numbers. Thus, at Mach numbers higher than the design one, the ramp shocks move inside the inlet and evolve into a strong incident shock, causing strong slip layers, remarkable total pressure loss, boundary-layer separation, and possible engine unstart. At Mach numbers lower than the design one, the ramp shocks move away from the cowl lip, causing loss of the precompressed airflow and the so-called spillage drag. To avoid these performance penalties at offdesign conditions, the control of the ramp shock system is needed. Therefore, variable geometric approaches for ramp shock control are widely considered and studied, such as the translating spike in the air turboramjet engine with expander cycle (ATREX) inlet [2], the rotatable ramps and variable diffusers in the hypersonic transport propulsion system research inlet [3], the variable length spike with multirow disks (MRDs) in the MRD disk inlet [4], the translating semiconic centerbody in the GTX inlet [5], etc. By regulating the ramp shocks according to the flight Mach number, variable geometry inlets can achieve a preferable aerodynamic performance in a considerably wide Mach number region. However, they have the drawbacks of increased vehicle weight, increased manufacturing complexity, decreased engine reliability, and decreased volumetric efficiency due to the need of moving devices, cooling passages, and sealing devices for moving components. These drawbacks are uneconomical to earth-to-orbit vehicles, because the additional dry weight must be carried to orbit and is detrimental to missiles, because they are typically characterized by light weight, simple structure, and disposable usage.

The design of hypersonic inlets may be much more convenient if a shock control technique characterized by fixed geometry is available. For example, one can design the inlet for a relatively low SOL Mach number and, at Mach numbers higher than the design one, move the ramp shocks from inside the inlet and back to the cowl lip by a shock control technique. Then, the mass flow ratio of the inlet can be substantially increased at low Mach numbers, and the length and weight of the inlet can both be decreased because of the reduction of the SOL Mach number and the absence of moving components. Therefore, the control of ramp shocks by fixed-geometry approaches, especially the magnetohydrodynamic (MHD) method, has generated a lot of interest in recent years. An attractive scenario for MHD inlet control has been put forward and analyzed by several groups [6–12]. With the aid of the artificially made plasma environment and an adjustable magnet located in the forebody, the method uses the Lorentz force to change the flow direction and achieves the control of the ramp shocks. Paper [11] has demonstrated that, while operating in the mode of net power extraction, this approach can yield an acceptable inlet performance. Paper [12] has predicted, by two-dimensional inviscid computations, that while operating in self-powered mode, this approach can restore the design shock configuration (Mach 5) in the Mach 8 flight. Overall, MHD control of the external shocks appears promising. However, due to the accompanying total pressure loss caused by the inevitable joule heating, the performance improvement of the MHD-controlled inlet is still not noticeable at several operating conditions. In consideration of the difficulty of air ionization at low-temperature conditions, this approach is especially uneconomical for a hypersonic inlet operating from Mach 4 to 6. Actually, from the viewpoint of a vehicle, the performance of the MHD-controlled inlet is further degraded because of the need of the plasma exciting device, the adjustable electromagnetic device, the energy storage unit, and the energy converter. Besides, the interference of the strong magnetic field could have formidable influence on the flight guidance and the radio communication of the vehicle. Jagadeesh et al. tries another method in [13]. He attempts to control the hypersonic flows around a flat plate by introducing a thermal boundary layer, called a thermal bump, through a high-energy spot within the boundary layer. But a comparison of the cases with and without thermal bump does not reveal any perceptible changes. Tan et al. suggests a fluidic shock control concept, by which an aerodynamically variable hypersonic inlet characterized by fixed geometry is devised [14]. The SOL condition is maintained from Mach 5 to 6, resulting in 20% extra captured air flow and 8% less forebody drag at low Mach numbers when compared with conventional fixed-geometry inlets.

The current paper builds upon the work of paper [14] and is devoted to develop a theoretical analysis and design method for the fluidic shock control technique, achieve a good knowledge of the underlying flow mechanism of the injection process, and demonstrate the shock control capability of this fluidic technique.

II. Description of the Fluidic Shock Control Concept

The fluidic shock control concept is schematically shown in Fig. 1. While the ramp shock needs to be controlled, a small quantity of secondary flow is introduced to the primary flowpath smoothly through a multihole or multislot plate installed at the forepart of the ramp. Because of the displacement effect of the mass addition, the effective aerodynamic boundary of the primary flow is deflected outward gradually, of which the forepart is concave and the rear part is convex. Therefore, a set of compression waves emanate from the concave portion of the aerodynamic boundary, and another set of expansion waves emanate from the convex portion of the boundary. These compression and expansion waves intersect the ramp shock in turn, and thus the ramp shock is bent outward and inward, correspondingly. The final result is that the ramp shock is pushed away from the ramp surface. Therefore, the position of the ramp shock relative to the cowl lip can be controlled by regulating the mass flow rate of the secondary flow through a valve. Because the introducing process of the secondary flow is performed in a distributed and mild manner, the accompanying unfavorable effects of traditional fuel injections in supersonic combustors, such as large total pressure loss and strong induced shocks, are basically absent. The driving pressure of the secondary flow is also fairly lower than that of fuel injections. Thus, the secondary flow can be drawn from the isolator or the successive ramps directly.

In addition to the ramp shock control, the injection of the secondary flow also brings some extra benefits. The injection of the secondary flow reduces the velocity gradient at the near-wall region and results in a decrease of the surface friction drag. If the secondary flow is precooled before the injection, the injectant evenly dispersed on the ramp surface can naturally act as a cooling film. What's more, according to the result of Berry et al. [15], the injection of the secondary flow can be regarded as fluidic distributed roughness, since vorticities are effectively induced within the boundary layer. Therefore, the injection of the secondary flow is also promising to develop into a forced boundary-layer transition method.

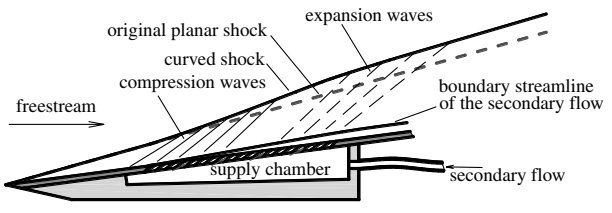

Fig. 1 Sketch of the fluidic shock control concept.

III. Theoretical Analysis of the Fluidic Shock Control Technique

A. Shock Control Requirement of a Generic Hypersonic Inlet

As shown in Fig. 2, the required displacements of the ramp shocks are first analyzed for a generic hypersonic inlet. The two-dimensional two-ramp inlet has an operating Mach number range of 4 to 6 and a SOL Mach number of M_{sh}. The shock control technique is used to push the ramp shocks outward to restore the SOL condition at Mach numbers higher than M_{sh}. Detailed design parameters of the hypersonic inlet are listed in Table 1.

According to the geometrical relations and the oblique-shock theory, one obtains the expressions for the maximum displacements of two ramp shocks at the duct entrance, which are expressed in terms of the maximum Mach number, the SOL Mach number, and two ramp angles:

$$h_{\mathrm{disp1}} = h_{\mathrm{Cap}} \cdot \frac{\sin(\beta_{1,M_{\mathrm{sh}}} - \beta_{1,M_{\max}})}{\sin\beta_{1,M_{\mathrm{sh}}} \cdot \cos(\beta_{1,M_{\max}} - \alpha_2)} \tag{1}$$

$$h_{\mathrm{disp2}} = h_{\mathrm{Cap}} \cdot \frac{\sin(\beta_{1,M_{\mathrm{sh}}} - \alpha_1) \cdot \sin(\beta_{2,M_{\mathrm{sh}}} - \beta_{2,M_{\max}})}{\sin\beta_{1,M_{\mathrm{sh}}} \cdot \sin\beta_{2,M_{\mathrm{sh}}} \cdot \cos(\beta_{2,M_{\max}} + \alpha_1 - \alpha_2)} \tag{2}$$

Varying M_{sh} from 4 to 6 and α_1 from 5 to 13° in Eqs. (1) and (2), a set of curves are obtained and plotted against the SOL Mach number in Fig. 3. In the calculation, h_{cap} is taken as 100 mm, and the second ramp angle is kept 19° to maintain a basically unchanged external compression amount for the inlet. As shown in Fig. 3, the required displacements of both ramp shocks decrease with the increase of the SOL Mach number. But the control of the first ramp shock is more demanding than that of the second one. While $M_{\mathrm{sh}} = 4.0$ and $\alpha_1 = 5°$, the maximum displacement of the first ramp shock reaches

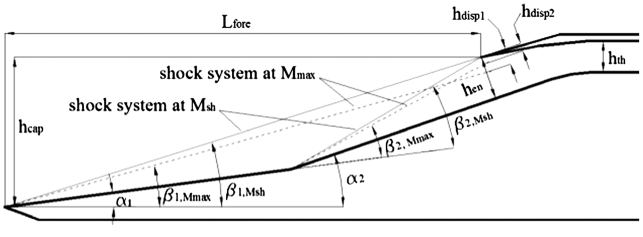

Fig. 2 Sketch of a generic hypersonic inlet.

Table 1 Design parameters of a generic hypersonic inlet

Parameter	Value
Starting Mach number	$M_{start} = 4$
Maximum Mach number	$M_{max} = 6$
SOL Mach number	M_{sh}
Theoretical capture height	h_{cap}
Height of duct entrance	h_{en}
Height of throat	h_{en}
Length of the forebody	L_{fore}
First ramp angle	α_1
Second ramp angle	α_2
Maximum displacement of first shock	h_{disp1}
Maximum displacement of second shock	h_{disp2}

as high as 27 mm. As to the effect of ramp angles, a larger first ramp angle can reduce the shock control requirement for the first ramp substantially, but it hardly affects that of the second ramp, although the flow-deviation angle of the second ramp decreases at the same time. The relations of the duct entrance height and the forebody length with the first ramp angle and the SOL Mach number are also shown in Fig. 3. The height of the duct entrance is found to be insensitive to the first ramp angle. The reason is that the air density and the flow Mach number at the duct entrance remain almost constant due to the basically unchanged external compression amount. The length of the forebody reduces continuously with the decrease of the SOL Mach number and the increase of the first ramp angle. The maximum length and the minimum length of the forebody in Fig. 3 are 420 and 211 mm, individually.

B. Shock Control Capability of an Attached Curved Surface on the Ramp Surface

The curved aerodynamic boundary of the primary flow, caused by the displacement effect of the secondary flow addition, can be taken as a curved solid surface if one neglects the difference of shear stress between a free shear layer and a wall-bounded shear layer. Therefore, compressible-flow theories are used to analyze the curved ramp shock and to obtain the shock control capability of an attached curved surface to the ramp surface.

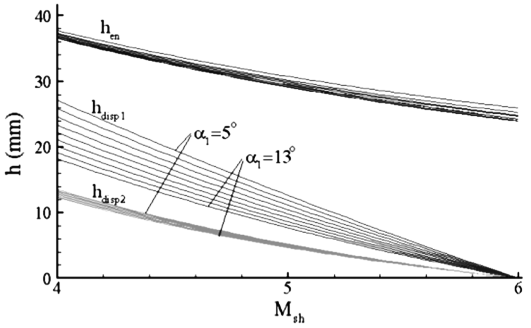

a) Entrance height of the duct and required displacements of two ramp shocks

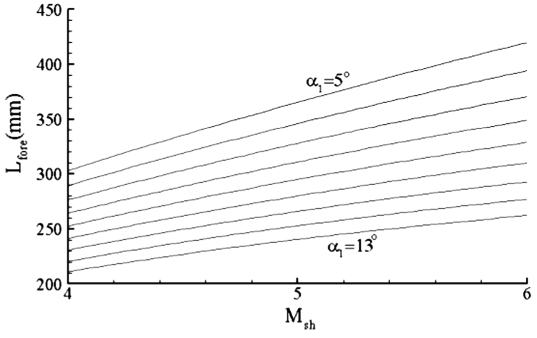

b) Length of the forebody

Fig. 3 Hypersonic inlets with different SOL Mach numbers and first ramp angles.

As shown in Fig. 4, the curved surface is divided into hundreds of straight segments. The flowfield is then calculated according to the oblique-shock theory and the Prandtl–Meyer supersonic-wave theory in a downstream-marching manner. When a weak wave intersects the ramp shock, a slip layer forms, and the pressure balance rule is used to determine the downstream pressure and the inclined angle of the succeeding segment of the curved shock. Thus, the profile, the displacement, the total pressure ratio, and the downstream Mach number of the curved shock can all be obtained. In theory, the weak compression waves and expansion waves downstream of the curved shock will bend locally due to the interference of slip layers. However, because the strength of these slip layers is rather weak, and the average Mach number of a weak wave is used in the calculation, the resultant error is actually negligible. Figure 5 presents a test case of curved shock prediction by this method. The freestream Mach number is 6.0, and the initial ramp angle is 7.5°. A two-dimensional Euler solver is used to provide the correct result. As can be seen, the predicted dashed line almost overlaps with the contour lines produced by the curved shock. Therefore, the analysis method for curved ramp shocks is reliable and will be used in the succeeding researches.

A parametric study is performed to obtain the shock control capability of a set of curved surfaces that are attached to an initial ramp. Table 2 lists the selected variables and the corresponding typical values. The S-shaped profiles are selected from [16] to represent three typical curving types, as shown in Fig. 6. The supposed hypersonic inlet has a maximum operating Mach number of 6, a SOL Mach number of 5, a theoretical capture height of 100 mm, and a total external turning angle of 19°. The analysis is conducted at Mach 6. A corrected ramp angle of 0.5° is used to take into account the effect of the forebody boundary layer. In each analysis process, only one variable is changed, and the others are kept constant.

The relations of the total pressure ratio and the displacement of the curved shock with the start position, the length, and the height of the curved surface are plotted in Fig. 7. As can be seen, the displacement of the first ramp shock increases monotonously with the upstream shift of the curved surface, the decrease of the surface length, and the increase of the surface height. There exists an upper threshold for the

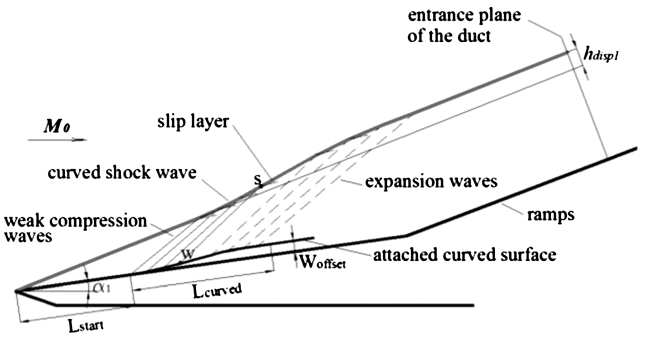

Fig. 4 Analysis of the curved shock of a ramp surface with an attached curved surface.

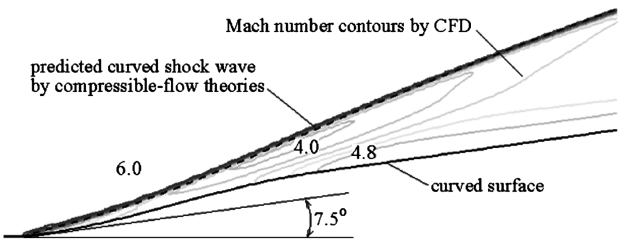

Fig. 5 Curved shocks obtained by theoretical analysis method and Euler solution.

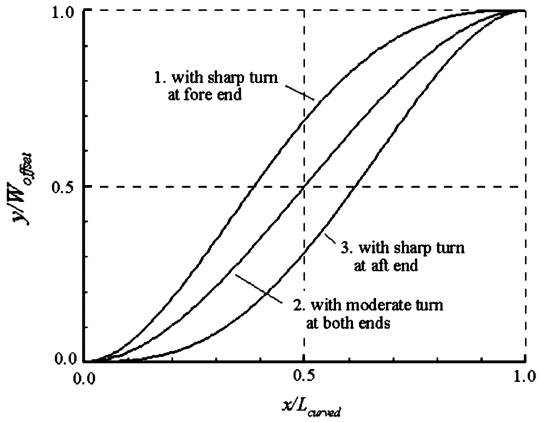

Fig. 6 Three curved surfaces with different profiles [16].

start position and the height of the curved surface and a low threshold for the length of the curved surface. When the design parameters are beyond these thresholds, compression waves converge in advance and develop into an oblique shock which intersects the ramp shock subsequently (Fig. 8). These situations are undesired due to the accompanying total pressure loss, although the ramp shock could be more efficiently displaced. According to this parametric study, the obtained maximum displacement of the ramp shock reaches as high as 22.9 mm. Recalling that the required shock displacement is 10.8 mm while $M_{\text{sh}} = 5.0, \alpha_1 = 7.5°$, according to Fig. 3a, the shock control capability is sufficient for a Mach 4 to 6 inlet with a SOL Mach number of 5. Figure 7 also shows that the total pressure loss of the curved ramp shock increases with the augment of shock displacement. This is easy to understand, since the increase of shock displacement implies a larger equivalent shock angle. In addition, the influence of surface profiles on the shock displacement is not pronounced, as shown in Table 3. Therefore, the profile with a sharp turn at the aft end is suggested for practical use to prevent an excessive adverse pressure gradient at the fore part of the attached curved surface.

C. Secondary Flow Rate Requirement and Injection Arrangement

While the shock control capability of the attached curved surfaces has been obtained, the subsequent critical issue is the realization of a given curved surface by distributed air injections. Since the displacement of the aerodynamic boundary of the primary flow is mainly caused by the mass addition effect of the secondary flow, the shape of the aerodynamic attached surface is decided by the distribution of the secondary flow along the ramp surface, and the maximum height of the attached surface is determined by the total amount of the secondary flow rate if interactions between the injected flow and the primary flow are neglected. Thus, the total amount and distribution of the secondary flow rate are two basic design factors of the fluidic shock control technique.

The total amount of the required secondary flow rate is estimated as follows. At first, the required shock displacement and the height of the corresponding attached surface can be calculated for a given hypersonic inlet, according to Sec. III.A. For example, the needed curved surface for the supposed hypersonic inlet in Sec. III.B is 3.9 mm in height. Then, according to Fig. 9, the required secondary-to-primary mass flow ratio can be expressed as

Table 2 Variables of the curved surfaces (refer to Fig. 4)

Parameter	Value
Initial ramp angle, α_1	7.5°
Start position, L_{start}	20 mm
Length, L_{curved}	100 mm
Height, W_{offset}	5 mm
Profile	S-shaped curve with moderate turn at both ends (Fig. 6)

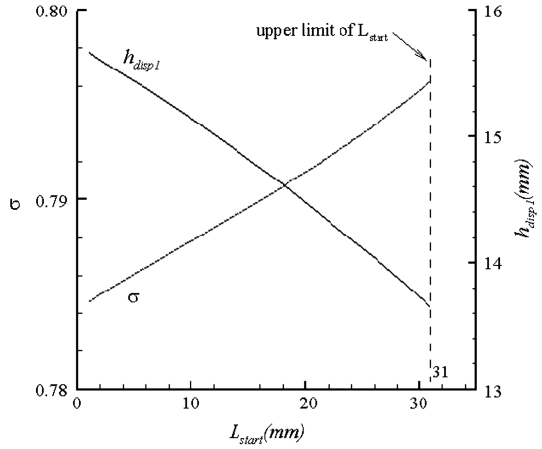

a) Influence of the start position

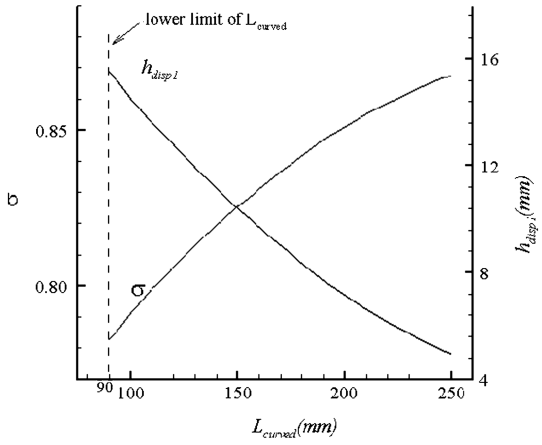

b) Influence of the length

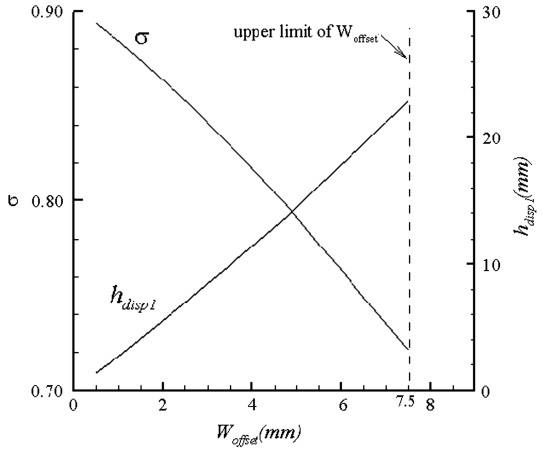

c) Influence of the height

Fig. 7 Influence of the curved surface parameters on the displacement and average total pressure ratio of the ramp shock.

$$\frac{\dot{m}_s}{\dot{m}_p} = \frac{\rho_s \cdot v_s \cdot L_{\text{curved}}}{\rho_1 \cdot u_1 \cdot h_1} = \lambda \cdot \frac{L_{\text{curved}}}{h_1} \tag{3}$$

where h_1 denotes the stream tube height of the primary flow after the first ramp shock, ρ_1 and u_1 are density and velocity of the primary flow after the first ramp shock, and ρ_s and v_s are the density and vertical injection velocity of the secondary flow, respectively. The nondimensional variable λ denotes the secondary blowing ratio and needs to be determined. For a zero pressure gradient boundary layer with distributed surface injection, the integrated momentum equation takes the form

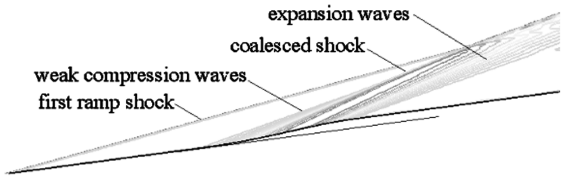

Fig. 8 Coalesced shock resulted from converged compression waves (CFD result, density contours).

$$\frac{\mathrm{d}\theta}{\mathrm{d}x} = \lambda \cdot \left(1 - \frac{u_s}{u_1}\right) + \frac{C_f}{2} \tag{4}$$

where u_s is the tangential injection velocity of the secondary flow, and C_f denotes the wall friction coefficient. C_f is negligible in the injection region, since the near-wall velocity gradient is fairly small. Also u_s can be neglected in comparison with u_1 if a porous wall is used to introduce the secondary flow. Therefore, integration of the simplified form of Eq. (4) yields

$$\theta_B - \theta_A = \lambda \cdot L_{\text{curved}} \tag{5}$$

where θ_A and θ_B are the momentum thickness at the start station and the end station of the injection block, respectively. Since the injection block is rather close to the leading edge of the ramp surface, θ_A can be ignored.

In addition, from the experimental data of McQuaid, which were obtained for incompressible boundary layers with distributed injection [17], a linear relation of the shape factor H_{imp} and the secondary blowing ratio λ can be established by a least-squares fitting method:

$$H_{\text{imp}}(\lambda) = 1.313 + 118.2 \cdot \lambda$$

This relation can be corrected for compressible boundary layers along an adiabatic wall, according to [18]:

$$H_{\text{comp}}(\lambda) = \frac{\delta_B^*}{\theta_B} = \left[0.129 + 0.648 \cdot \left(\frac{k-1}{2} \cdot M_1^2\right) + 0.871 \cdot \left(1 + \frac{k-1}{2} \cdot M_1^2\right)\right] \cdot H_{\text{imp}}(\lambda) \tag{6}$$

Notice that M_1 cannot be calculated directly from the freestream Mach number and the first ramp angle, since the ramp shock transforms into a curved shock. In Eq. (6), δ_B^* denotes the displacement thickness of the equivalent boundary of the primary flow and ought to be the sum of the displacement thickness of the noninjection state ($\delta^*_{B,\text{noninjection}}$) and the height of the attached curved surface (W_{offset}). According to the following equation, $\delta^*_{B,\text{noninjection}}$ can be estimated [18]:

$$\delta^*_{B,\text{noninjection}} = \delta^*_{\text{noninjection,imp}} \cdot \left[0.129 + 0.648 \cdot \left(\frac{k-1}{2} \cdot M_1^2\right) + 0.871 \cdot \left(1 + \frac{k-1}{2} \cdot M_1^2\right)\right] \cdot \left(1 + \frac{k-1}{2} \cdot M_1^2\right)^{-0.6} \tag{7}$$

where

$$\delta^*_{\text{noninjection,imp}} = 0.0504 \cdot \frac{x_B}{(Re_{x_B})^{0.2}}$$

Table 3 Shock displacement of different surface profiles

Profile description [16]	Shock displacement, mm
Sharp turn at aft end	14.7
Adequate turns at both ends	14.5
Sharp turn at fore end	15.8

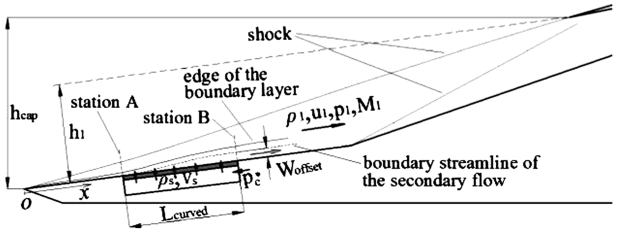

Fig. 9 Estimation of the required secondary-to-primary mass flow ratio.

For the current case, M_1, L_{curved}, W_{offset}, and $\delta^*_{B,\text{noninjection}}$ are 4.67, 100, 3.9, and 1.1 mm, respectively. Thus, λ can be determined by Eqs. (5) and (6) and is calculated to be 0.00374.

Finally, substituting the values of λ, h_1 (57.48 mm), and L_{curved} into Eq. (3) yields

$$\dot{m}_s/\dot{m}_p = 0.65\%$$

The next step is to obtain an attached curved surface aerodynamically by arranging the slots of the injection block.

An injection scheme characterized by the constant slot width and variable slot interval is proposed to introduce the secondary flow smoothly. As shown in Fig. 10, the desired attached surface is divided into n segments in equal height. For each segment, the displacement will be achieved by an equal amount of air injection. Therefore, injection slots in equal width (Δ) are placed at the center of each segment. These slots are spaced unevenly along the ramp surface, since the slope of the attached curved surface varies. In addition, in order to depict the slow turns at both ends of the surface, the first segment and the last segment are subdivided into three subsegments, of which one is $y/(W_{\text{offset}}2n)$ in height and the other two are $y/(W_{\text{offset}}4n)$ in height. Therefore, injection slots for these subsegments are $\Delta/2$ and $\Delta/4$ in width, respectively.

At last, the total width of the injection slots ($W_{\text{slot}} = n \times \Delta$) needs to be estimated. For the supposed hypersonic inlet, according to conservation of mass, one obtains

$$p_1 \cdot [1 + (k-1) \cdot M_1^2/2]^{k/(k-1)} \cdot q(M_1) \cdot h_1 \cdot 0.65\% = p_c^* \cdot W_{\text{slot}} \cdot Q \tag{8}$$

Substituting $M_1 = 4.67$ and $h_1 = 57.48$ mm into Eq. (8) gives

$$W_{\text{slot}} = \frac{6.98}{Q \cdot p_c^*/p_1} \text{ mm} \tag{9}$$

where Q denotes the mass flow coefficient of the multislot plate, and p_c^* is the total pressure of the secondary flow in the supply chamber. As shown in Eq. (9), the total width of the slots is in inverse ratio to

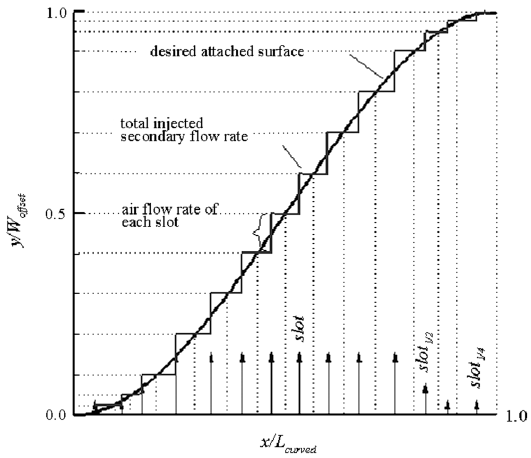

Fig. 10 Arrangement of the injection slots for a prescribed curved surface.

p_c^*/p_1 and Q. If the chamber pressure ratio of the secondary flow is 1.75 and a streamwise injection scheme is used, the mass flow coefficient of the multislot plate is about 0.4 [19]. Substituting these values into Eq. (9) yields $W_{\text{slot}} = 10$ mm.

D. Computational Fluid Dynamics Verification of the Theoretical Analysis and Design Method

To verify the theoretical analysis and design method for the fluidic shock control technique, a control scheme of the first ramp shock is designed and numerically studied in combination with the supposed hypersonic inlet in Sec. III.B. Table 4 lists primary parameters of the fluidic shock control scheme.

A three-dimensional N–S solver is used to calculate the flowfield, which is two-dimensional in nature; thus, only three layers of mesh are placed along the spanwise direction. The effectiveness of this solver has been widely verified for the calculations of hypersonic inlet flow [20,21]. In solving the flow equations, a point Gauss–Seidel scheme is used to perform time marching, and Roe's scheme in combination with the MUSCL interpolation method is used to obtain the inviscid fluxes at the control surfaces. To alleviate the numerical stiff problem possibly encountered in the calculations of the chamber flow, a time-derivative preconditioning technique is also adopted. The turbulent flow is modeled by the nonlinear renormalization group k-ε model, of which the governing equations are discretized by a second-order upwind scheme. Also, standard wall functions are introduced to model the near-wall region flow.

The computational domain includes the flowfields surrounding the hypersonic inlet, in the supply chamber and in the injection slots. A structured mesh composed of 277,200 hexahedral elements is used for both calculations of the injection case and the noninjection case. The surface on the right side of the supply chamber is set as a pressure inlet boundary for the injection case and as an adiabatic wall boundary for the noninjection case. The y^+ values of most near-wall cells are found in the range of $20 \sim 80$.

Numerical investigation is performed at a freestream Mach number of 6.0 and a flight altitude of 25 km. The convergence of each run is decided according to the residual history of each governing equation. When the residual of each equation drops gout orders of magnitude and the mass flow rates of both the secondary flow and the primary flow are stable, the calculation is considered converged. The value of p_c^* is adjusted repeatedly to ensure that the first ramp shock hits the cowl lip precisely. In Fig. 11, the computational fluid dynamics (CFD)-obtained Mach number contours, while the injection is on and off, are both illustrated and accompanied by the boundary streamline of the secondary flow, the equivalent aerodynamic boundary of the primary flow $\delta^*(x)$, and the variation of the displacement thickness caused by the injection $\Delta\delta^*(x)$. As it can be seen, the injected secondary flow does work in the prearranged manner, compelling the aerodynamic boundary of the primary flow to deflect outward smoothly and forcing the ramp shock that otherwise would enter the duct to bend toward the cowl lip. Obviously, $\Delta\delta^*(x)$ describes the shape of the aerodynamic attached surface and determines the shock control capability. From the enlarged view in Fig. 11, it can be noticed that the aerodynamic attached surface is rather close to the boundary streamline of the secondary flow. That's to say, the realization of aerodynamic attached surface mainly depends on the mass addition effect of the secondary flow, and the vertical momentum of the injected flow just plays a negligible role. A further analysis of CFD results shows that the aerodynamic boundary of the primary flow is displaced by 4.85 mm, which is 8.4% of h_1, at the cost of a secondary-to-primary ratio of 0.8%. The displacement effect of the secondary flow is amplified by more than 10 times if one regards that its flow capability is the same as the primary flow. This is mainly because the flow capability of the secondary flow is decreased substantially by its low-injection velocity and density. Downstream of the injection block, the injected flow obtains energy from the primary flow through the work of viscous shear stress and accelerates gradually; thus, the boundary streamline deflects to the wall slowly. The boundary streamline is further compressed to the wall by the second ramp shock. At the entrance of the duct, the passage of the secondary flow occupies only 2.96% of the duct height and 19.7% of the local boundary-layer thickness. Therefore, the process of mass addition will not bring an apparent unfavorable effect to the internal flow.

In Fig. 11, the predicted curved shock and the desired curved surface are also plotted in a solid black line to verify the correctness of the analysis and design method. In general, the predicted curved shock agrees well with the numerically obtained one, although a slight discrepancy, which is possibly caused by the viscous interaction of hypersonic boundary flow near the leading edge, can still be observed at the foot region of the shock. As to the aerodynamic attached surface, the CFD-obtained profile, $\Delta\delta^*(x)$, basically overlaps the desired surface profile at the forepart of the injection region, but it deviates from the latter slowly at the aft part of the injection region. This discrepancy may be a result of the strong interference of the external pressure gradient in the streamwise direction, which is not included in the theoretical analysis model. At the aft part of the injection region, the local injection flow rate becomes small, but an expansion fan appears (Fig. 1) and re-accelerates the boundary flow. The velocity profile of the mixed boundary layer thus becomes more uniform, and the corresponding shape factor H decreases. Therefore, the displacement thickness decreases and the boundary of the aerodynamic attached surface turns toward the ramp surface, although the momentum thickness increases monotonously along the flow direction. However, the discrepancy of the aerodynamic boundaries will not apparently affect the obtained shock displacements, since the major portion of the expansion fan enters the duct.

Typical parameters of the injection process are listed in Table 5 to examine the theoretical analysis method further. The CFD-obtained results show that the chamber pressure ratio is 1.8, a little higher than

Table 4 Primary design parameters of the fluidic shock control scheme

Parameter	Value
SOL Mach number of the supposed inlet, M_{sh}	5.0
Maximum operating Mach number of the supposed inlet, $M_{\max}$	6.0
First ramp angle, α_1	7.5°
Theoretical capture height of the supposed inlet, h_{cap}	100 mm
Entrance height of the supposed inlet, h_{en}	29.2 mm
Required displacement of the first ramp shock at the duct entrance, h_{disp1}	10.8 mm
Height of the attached curved surface, W_{offset} (predicted value)	3.9 mm
Secondary-to-primary mass flow ratio, $\dot{m}_s/\dot{m}_p$ (predicted value)	0.65%
Length of the injection region, L_{curved}	100 mm
Start position of the injection region, L_{ramp}	20 mm
Injection angle of the secondary flow	30°
Chamber pressure ratio of the secondary flow, p_c^*/p_1	1.75
Total width of the injection slots, W_{slot}	10 mm
Count of the divided segments, n	10
Relative position of each slot, x/L_{curved}	0.05, 0.11, 0.16, 0.24, 0.32, 0.40, 0.47, 0.53, 0.60, 0.67, 0.76, 0.83, 0.88, 0.95

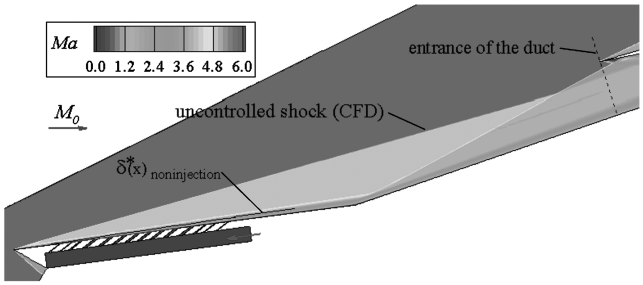

a) Injection off

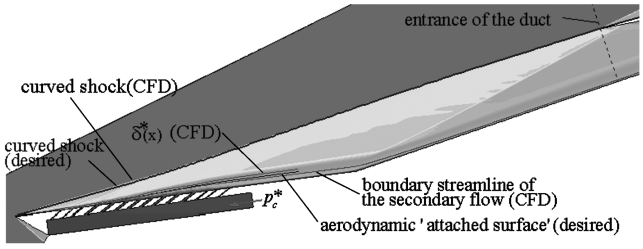

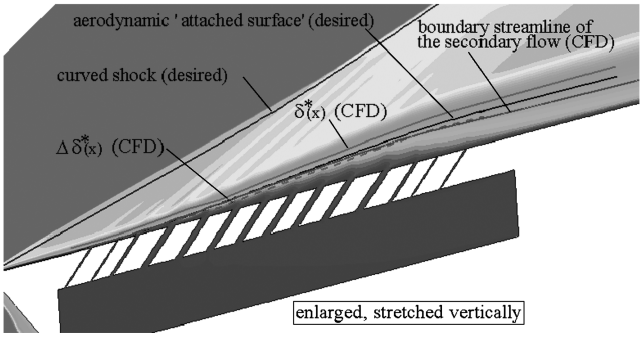

b) Injection on

Fig. 11 Control effects of the fluidic shock control technique (predicted and CFD results).

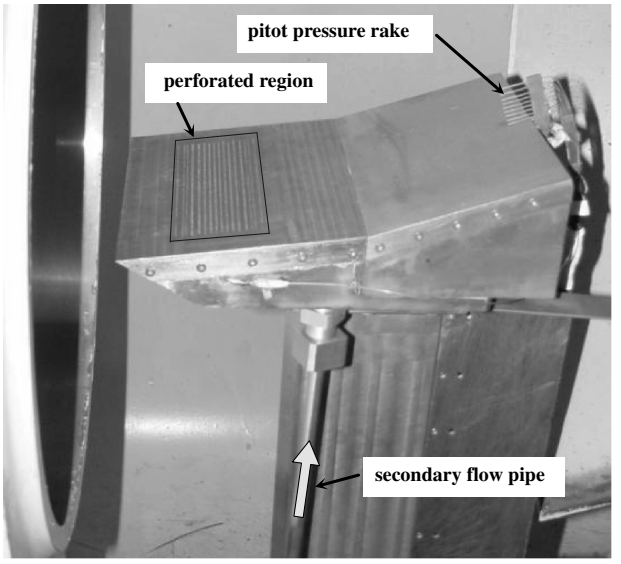

a) Test model installed in the wind tunnel

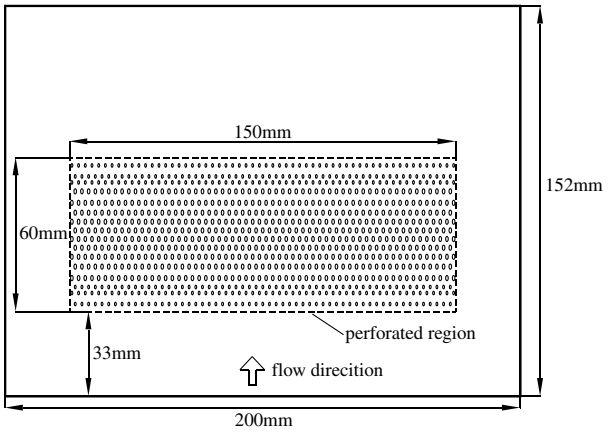

b) Sketch of the multihole plate

Fig. 12 Test model for the fluidic shock control technique.

the designed one (1.75), and the secondary-to-primary mass flow ratio is not 0.65%, as predicted, but 0.80%. From other parameters listed in Table 5, one can find that the prediction error of the mass flow ratio mainly comes from the estimation of the momentum thickness of the boundary layer at station B. The theoretical analysis method overpredicts the influence of the air injection on the development of the momentum thickness substantially, giving a larger momentum thickness at a smaller secondary-to-primary mass flow ratio. A further analysis shows that it is the neglect of the tangential injection velocity in Eq. (4) that mainly contributes to this overprediction. According to the CFD result, the tangential injection velocity is fairly high, while a slot injection scheme, not a porous injection scheme, is adopted. The typical value of u_s/u_1 for the current case is about 0.16. In fact, a much better predicted value of the secondary-to-primary mass flow ratio, 0.75%, can be obtained if one takes the tangential injection momentum into account and uses the CFD-obtained value of u_s/u_1. In addition, the predicted values of $\delta^*_{B,\text{noninjection}}$, $\Delta\delta^*_B$, and H_B are also somewhat different from the corresponding values obtained by CFD. For example, the displacement thickness of the boundary layer at station B for the noninjection case is estimated to be 1.1 mm, according to Eq. (8), much smaller than the CFD-obtained one. The main reason for this discrepancy is that the surface roughness formed by the slots is not included in Eq. (8). As to $\Delta\delta^*_B$, the prediction error mainly comes from the interference of the external pressure gradient, which is already explained in the previous paragraph.

In summary, the analysis and design method developed in this section makes a framework for the fluidic shock control technique. This method can provides reasonable results for the prediction and design of the injection process, although the accuracy needs to be improved from several aspects, such as including the effects of the tangential injection momentum, the surface roughness caused by the injection slots, etc.

Table 5 Typical parameters of the injection process (Predicted and CFD results)

Parameter	Predicted result	CFD result
Secondary-to-primary mass flow ratio, $\dot{m}_s/\dot{m}_p$	0.65%	0.80%
Chamber pressure ratio, p_c^*/p_1	1.75	1.80
Momentum thickness of the boundary layer at station B, θ^*_B	0.37 mm	0.33 mm
Displacement thickness of the boundary layer at station B, δ^*_B	5.00 mm	4.85 mm
$\delta^*_{B,\text{noninjection}}$	1.1 mm	1.6 mm
$\Delta\delta^*_B$	3.9 mm	3.25 mm
Shape factor of the boundary layer at station B, H_B	13.51	14.70

IV. Demonstration of the Fluidic Shock Control Technique by Wind-Tunnel Tests and Three-Dimensional Computations

A. Description of the Test Model

To demonstrate the effectiveness of the fluidic shock control technique and verify the CFD tool, a test model is designed and fabricated. As shown in Fig. 12, the model embodies two ramps of a generic hypersonic inlet and can demonstrate the control of the first ramp shock. The inclined angles of the two ramps are 7.5 and 19.0°, respectively. The supposed inlet is designed for a SOL Mach number of 5.0 and has a theoretical capture height of 78.5 mm. The corresponding height of the duct entrance is 23.8 mm. While the freestream Mach number is increased to 5.74, the required displacement of the first ramp shock is 6.4 mm at the duct entrance of the supposed inlet.

The test model is 272 mm in length and 200 mm in width. A multislot plate is aborted during the design process of the test model, since the narrowest slot is just 0.12 mm in width, which adds the manufacturing difficulties and increases the possibility of dust blockage. Instead, a multihole plate with a perforated region 60 mm in length and 150 mm in width is used. The perforated region is placed 33 mm downstream of the leading edge of the first ramp and contains 16 staggered rows of circle-inclined holes. Each row consists of 57 holes and has the same flow area as the original slot. These holes are not quite uniform. The diameters of the typical holes are 1.0 mm, while for the other holes, the diameters are 0.5 mm (row 1, 2, 15, and 16) and 0.7 mm (rows 3 and 14). The row-to-row distance in the streamwise direction is determined by the design method in Sec. III.C, which ensures that the injected secondary flow rate increases according to an S-shaped profile. In detail, the distance from the leading edge of the first ramp to each row is 36.0, 40.3, 42.6, 46.1, 50.6, 54.4, 58.0, 61.3, 64.7, 68.1, 71.6, 75.5, 79.9, 83.4, 85.7, and 90.0 mm. The hole-to-hole distance in the spanwise direction remains constant (2.6 mm). The angle relative to the ramp surface of each hole is 30°. During the tests, the secondary flow is derived from the ambient air, since the static pressure of the test chamber is only about $1 \sim 2$ kPa. The air is transferred to the supply chamber beneath the first ramp surface and then injected into the primary flow through the inclined holes. An air valve is installed on the delivery pipe outside the test chamber to regulate the mass flow rate manually.

In addition, a pitot pressure rake and a surface pressure tap are placed at the duct entrance of the supposed inlet. In the supply chamber, four static pressure taps are arranged to obtain the total pressure of the injected secondary flow (p_c^*).

B. Experimental Conditions, Measurements, and Numerical Approach

All experiments are conducted in the hypersonic wind tunnel of the Nanjing University of Aeronautics and Astronautics. The facility runs in a blown-down mode with a usable runtime greater than 7 s. The test chamber is fully closed, with two embedded glass windows (300 mm in diameter) for optical access. Upstream of the test chamber, an interchangeable converging–diverging nozzle with an exit diameter of 500 mm is located, providing nominal freestream Mach numbers from 5.0 to 8.0 and flight conditions from 27 to 59 km. For current experiments, the Mach 6 nozzle is used, and the corresponding flow conditions are summarized in Table 6. The schlieren visualization technique is used to capture the profile of the curved shock, and the image resolution is 800×600 pixels. All pressures are measured by an electronically scanned pressure transducer system (ESP). The pressures obtained by the ESP have a margin error of 0.05% over the full range of calibration.

The Navier–Stokes (N–S) solver stated in Sec. III.D is used to conduct these three-dimensional simulations, and the calculation setting is also the same. Since the flowfield is periodic along the spanwise direction, the computational domain is chosen to contain only one and two half-columns of injection holes, as shown in Fig. 13. The entire computational domain is filled with hexahedral elements that cluster near the wall region and the shock wave region (Fig. 14). The height of the near-wall cells are adjusted to keep most y^+ values larger than 20 and less than 100, since standard wall functions are adopted by the turbulence model. At two sides of the computational domain, periodic boundaries are used.

Table 6 Test conditions for the fluidic shock control technique [22]

Property	Value
Nominal Mach number	6
Actual Mach number	5.74
Total temperature, K	$540 \sim 550$
Total pressure, 10^6 Pa	$1.1 \sim 1.2$
Usable runtime, s	>7
Diameter of the uniform flow region at the station of 300 mm downstream of the nozzle exit, mm	>300

Grid sensitivity analysis is performed with three grids of increasing resolution. For each grid size, the grid topology is the same. The obtained results are listed in Table 7, with the experimental value. As it can be seen, the difference between the medium grid and the fine grid is 1.8% for the secondary-to-primary mass flow ratio and 2.5% for the ramp shock displacement. That is to say, the truncation errors involved in the numerical analysis are acceptably small for the medium grid. Thus, a grid of 2,277,200 cells is adopted in the subsequent numerical analysis.

C. Results and Discussion

Tests and computations are performed at a freestream condition of $M_0 = 5.74$. At first, the air valve on the delivery pipe of the secondary flow is closed to obtain the uncontrolled case for reference. In computations, the uncontrolled case is simulated by setting the right surface of the supply chamber as an adiabatic wall boundary. The corresponding results obtained by experiments and computations are shown in Fig. 15. As can be seen, due to the absence of air injection, two ramp shocks converge upstream of the measurement plane and then develop into a strong oblique shock, issuing a clear slip layer. By prolonging the first ramp shock to the measurement plane, one can obtain the shock-to-wall distance at the duct entrance, of which the experimental value is 17.6 mm and the computational one is 18.0 mm. In consideration of the pronounced static pressure gradient at the measurement plane, pitot pressures are not converted into total pressures, to preserve the accuracy of the experimental data. Instead, the CFD-obtained total pressures are converted into pitot pressures, and shown in Fig. 15c, together with the experimental data, to provide comparisons. An abrupt change in the pitot pressure coefficient is found between the sixth and seventh tubes, indicating the impingement of the coalesced shock between them. In addition, the computed pitot pressure coefficient agrees well with the experimental data at the entire measurement plane. Taking the eighth tube, which is exposed directly to the freestream (for example), the pitot coefficients obtained by experiment and computation are 0.0357 and 0.0359, respectively. These values are also very close to

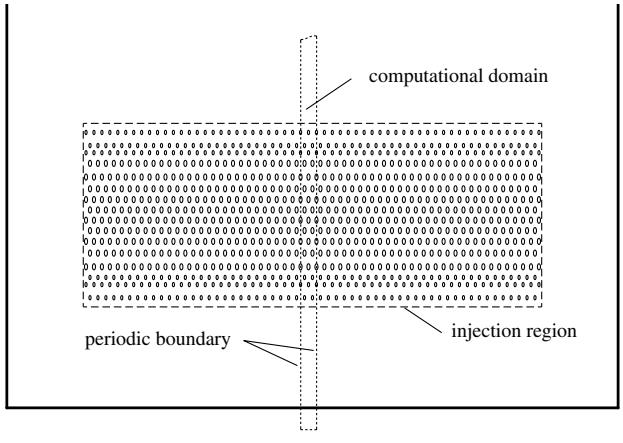

Fig. 13 Computational domain.

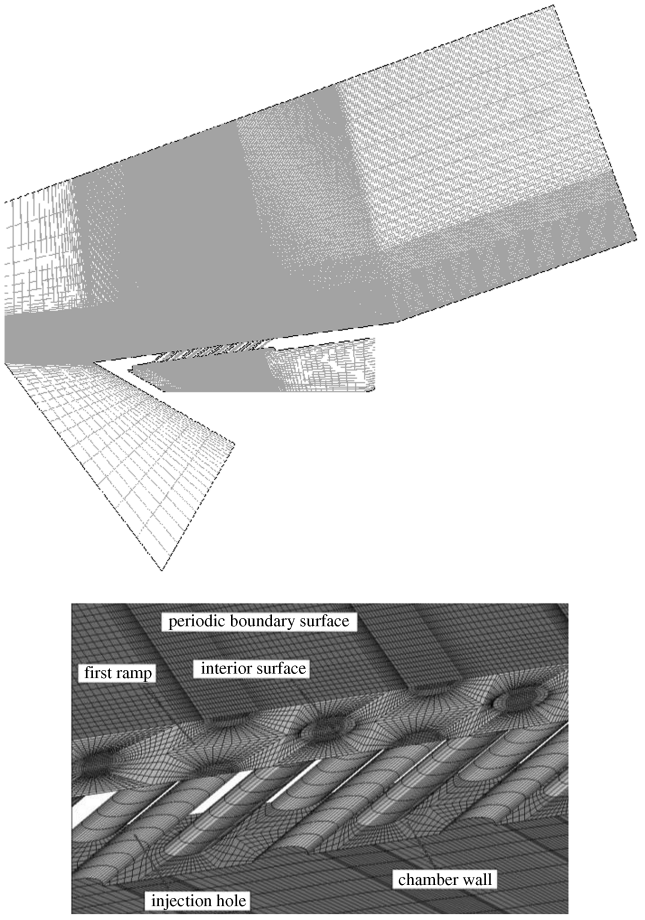

Fig. 14 Computational mesh.

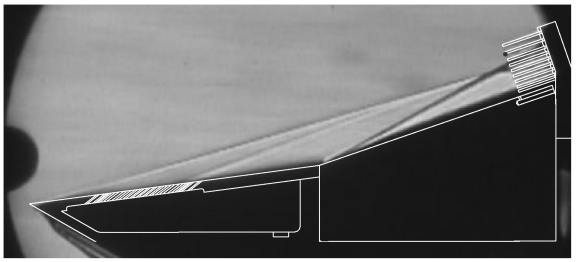

a) Schlieren photograph

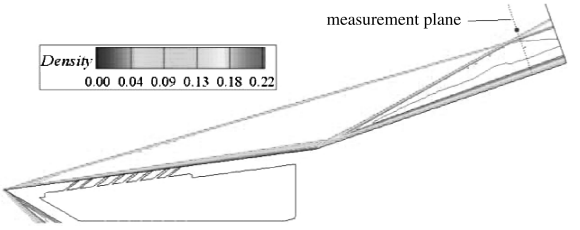

b) Computed density contours

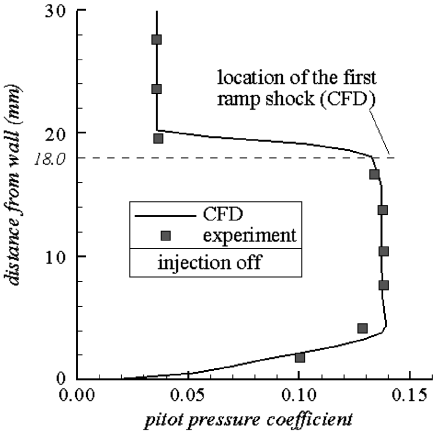

c) Distribution of pitot pressure coefficient at the measurement plane

Fig. 15 Flow pattern of the forebody flowfield and pitot pressure distribution of the measurement plane while the air injection is closed.

the theoretical one, 0.0356, of the total pressure ratio across a normal shock of Mach 5.74 flow.

The air valve is gradually opened to demonstrate the control of the first ramp shock. Figure 16 presents the obtained results while the pressure ratio (p_c^*/p_1) of the supply chamber is 1.55. The secondary-to-primary mass flow ratio is 0.56%, according to the corresponding CFD simulation. Both the schlieren photograph and the calculated contours show that, due to the displacement effect of the secondary flow, the boundary layer downstream of the injection block apparently thickens, and the first ramp shock leaves the second ramp shock and bends toward the cowl lip (shown by a dot in Fig. 16). The corresponding shock-to-wall distance is 22.6 mm by experiment and 21.5 mm by computation. The schlieren photograph also shows that an induced shock occurs directly upstream of the injection region. This phenomenon is predicted by neither the theoretical analysis nor by the CFD computation. The theoretical analysis indicates that weak compression waves do not converge beneath the first ramp shock until the secondary-to-primary mass flow ratio reaches 0.98%. Three-dimensional simulation shows that no evident coalesced shock is observed, even at a secondary-to-primary mass flow ratio of 1.11%. The discrepancy between the experiment, the theoretical analysis, and the CFD simulation may be related to boundary-layer separation on the first ramp. In experiments, laminar separation of the boundary layer may appear around the first row of holes and induce an extra shock. However, in the analysis method, a nonseparation model is used, and in the CFD simulation, the entire boundary flow is regarded as turbulent. Thus, neither method can predict the laminar separation. The induced shock intersects the first ramp shock and produces an extra shock displacement of 1.1 mm as compared with the CFD result. A slip layer is also observed issuing from the intersection point, according to the schlieren photograph. Nevertheless, no evident extra total pressure loss is found, since the induced shock is rather weak, which can be inferred from the good consistency of the experimentally and numerically obtained pitot pressure coefficients. Figure 16 also shows that the seventh pitot tube happens to lie between the first and the second ramp shocks; thus, another plateau appears on the distribution of the pitot pressure coefficient.

The air valve is opened further until the pressure ratio of the supply chamber increases to 2.50 (Fig. 17). According to the CFD

Table 7 Grid sensitivity analysis for the fluidic shock control test ($p_c^*/p_1 = 1.55$)

Run	No. of cells	Secondary-to-primary mass flow ratio	Displacement of the first ramp shock, mm
Coarse	1,282,200	0.56%	3.5
Medium	2,277,200	0.56%	3.9
Fine	4,405,800	0.55%	4.0
Experimental value	——	——	5.0

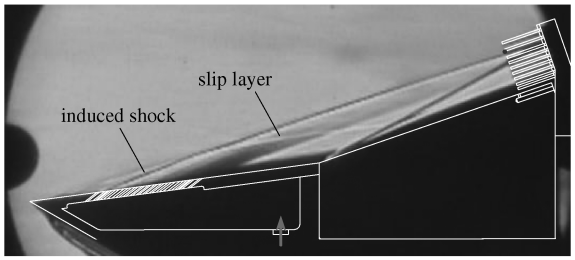

a) Schlieren photograph

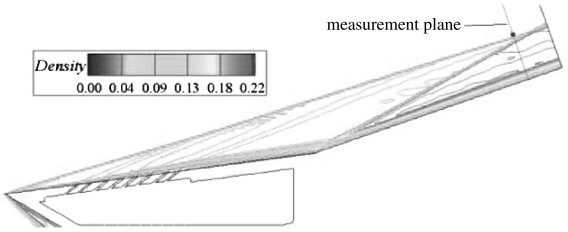

b) Computed density contours

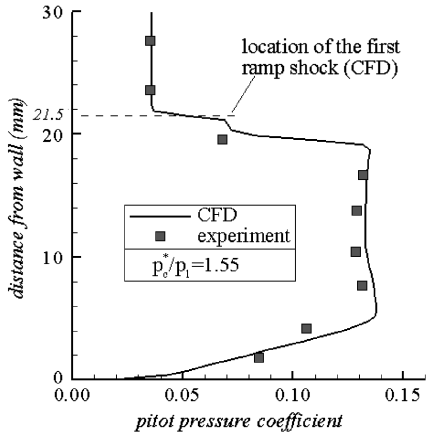

c) Distribution of pitot pressure coefficient at the measurement plane

Fig. 16 Flow pattern of the forebody flowfield and pitot pressure distribution of the measurement plane at a chamber pressure ratio of 1.55.

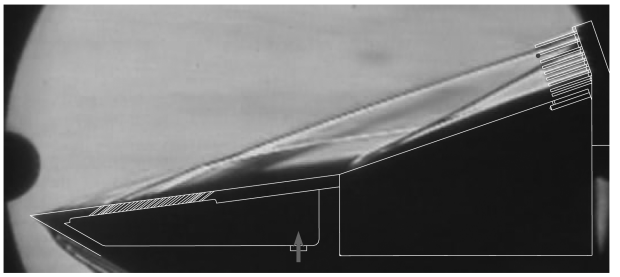

a) Schlieren photograph

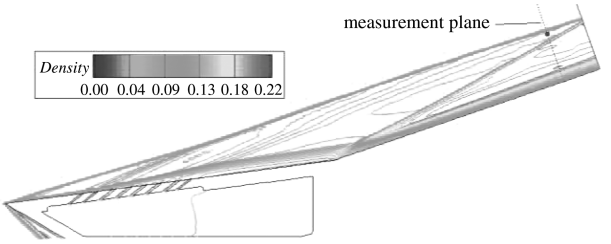

b) Computed density contours

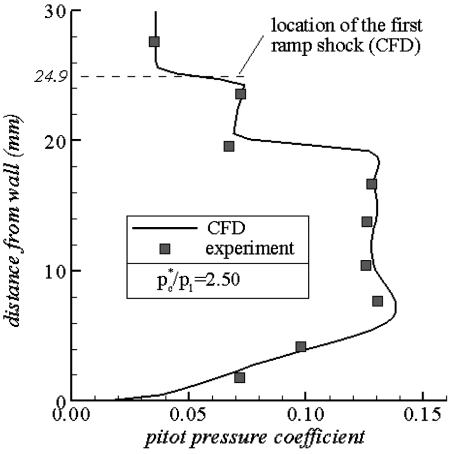

c) Distribution of pitot pressure coefficient at the measurement plane

Fig. 17 Flow pattern of the forebody flowfield and pitot pressure distribution of the measurement plane at a chamber pressure ratio of 2.50.

simulation, the corresponding secondary-to-primary mass flow ratio is 1.11%. Because of the increased displacement effect of the secondary flow, the first ramp shock continues to bend outward, gets across the cowl lip, and moves to the lip of the ninth pitot tube. The shock-to-wall distance at the measurement plane is 26.3 mm by experiment and 24.9 mm by CFD simulation. That is, the experimentally obtained displacement of the first ramp shock reaches 8.7 mm at the measurement plane. The pitot pressure coefficient of the eighth tube stays at the same plateau as that of the seventh tube, since the first ramp shock has moved outside. In addition, although the boundary layer thickens substantially, the downstream flow remains fairly stable, and no shock/boundary-layer interaction is observed.

In addition, the three-dimensional effects of the multihole injection process are examined according to the CFD results at a chamber pressure ratio of 1.55. The boundary streamlines and the corresponding stream tubes, which are released from the first to the sixth rows of injection holes, are displayed in Fig. 18. The local Mach number distributions on these stream tubes are also shown with a banded color map. As can be seen from Fig. 18a, due to the impact of the external flow, the secondary flow is confined within a thin layer near the ramp surface after the injection through inclined holes, which is the same as the slot injection. But the front view of these stream tubes in Fig. 18b indicates that the injection process of the secondary flow embodies strong three-dimensional features. As a result of the impingement of the upstream coming flow and the downstream injected flows, the outlines of the stream tubes are rather similar to those of a lotus root, expanding and shrinking periodically in width, and the cross-sectional shape of each tube is crescent, with the top surface protruding upward substantially. Therefore, several sinuous and narrow flow passages, which will be filled by the primary flow, form between each of the two adjacent stream tubes. Figure 19b also shows that the injection Mach number of the secondary flow is fairly low: less than 1.0. But after the injection, the secondary flow gains energy continuously from the primary flow and, at the end of the injection block, the flow Mach number reaches as high as 2.0.

Streamlines and the corresponding stream surfaces, which are released from three spanwise lines placed in the boundary layer immediately upstream of the injection block, are shown in Fig. 19 to demonstrate the response of the primary flow. The distances from the wall of these lines are 0.01, 0.5, and 1.0 mm, and the corresponding stream surfaces are marked by A, B, and C, respectively. As can be seen, stream surface A, which is nearest to the injected secondary flow, is substantially affected by the three-dimensional features of the injection process. It bends and curves around the stream tubes of the secondary flow to fill in the gap between them. However, after the buffering of the boundary-flow cushion, which is about 0.5 mm thick, stream surface B is much smoother. The sinuous motion along the streamwise direction disappears, and only a mild fluctuation in the spanwise direction can be observed. The Mach number

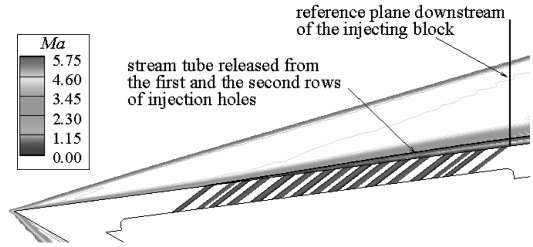

a) Side view

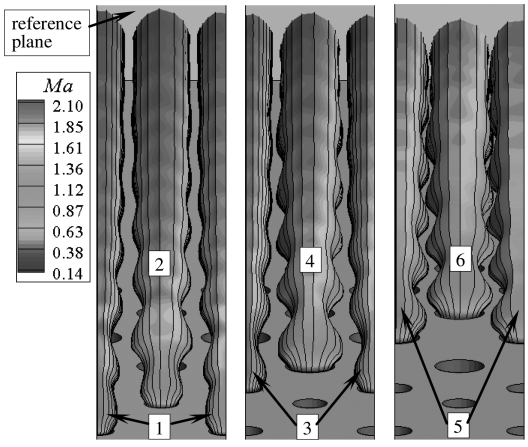

b) Front view

Fig. 18 Stream tubes released from the first to sixth rows injection holes.

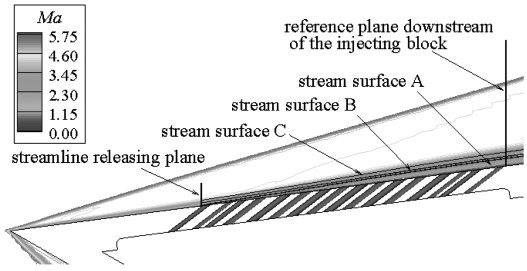

a) Side view

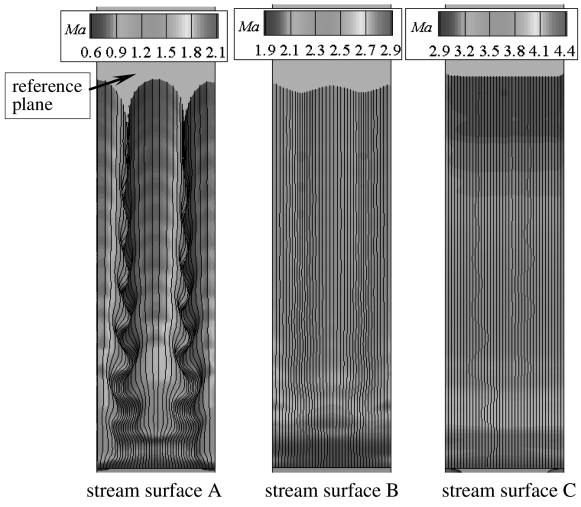

b) Front viw

Fig. 19 Stream surfaces released from three spanwise lines.

distribution on stream surface B is also more even in the spanwise direction. As to stream surface C, the three-dimensional features, especially in the spanwise direction, almost vanish, indicating that the three-dimensional features of the injection process will not bring additional influence on the high-speed primary flow. Therefore, the curved ramp shock and the flow process above the boundary layer are still two-dimensional in nature. What's more, since the displacement of the aerodynamic boundary of the primary flow mainly depends on the mass addition effect of the secondary flow, the injection style, by slots or holes, should not apparently affect the aerodynamic boundary displacement of the primary flow. To sum up, the three-dimensional features of the injection process will not change the shock control capability of the secondary flow. In fact, the theoretical analysis method developed in Sec. III.C is used to estimate the required secondary-to-primary mass flow ratio under the test condition. The predicted secondary-to-primary mass flow ratio is 0.49%. Recalling that the corresponding CFD value is 0.56%, the predicting error is even smaller than the two-dimensional case in Sec. III.D.

V. Conclusions

This paper involves a fluidic shock control technique, characterized by fixed geometry, to facilitate the design of hypersonic inlets. A theoretical analysis and design method, which is devoted to the prediction and arrangement of the secondary flow injection, is developed and verified by CFD computations. Also, a test model is designed and tested to demonstrate the shock control capability of this fluidic technique and verify the CFD tool.

Since the control of the first ramp shock is more demanding than that of the second ramp shock, the current study mainly focuses on the control of the first ramp shock. First, the displacement effect of the distributed air injection is taken as an attached S-shaped surface by neglecting the interactions between the injected flow and the primary flow. Then, a parametric study of a set of curved surfaces is conducted according to the compressible-flow theories to obtain the shock control capability. Therefore, for a specific shock control requirement, the height of the corresponding attached curved surface can be determined. Then, the required secondary-to-primary mass flow ratio is calculated according to the integrated momentum equation and the empirical formula of the shape factor with the secondary blowing ratio. Finally, a design method of the air injection scheme, which is characterized by the constant slot width and variable slot interval, is brought forward to compose a prescribed curved surface aerodynamically and realize the desired shock displacement.

The correctness of the theoretical analysis and design method and the underlying flow mechanism are verified by CFD with a two-dimensional case. As compared with the noninjection case, an aerodynamic curved surface is found attached to the ramp surface while the air injection is opened; thus, the ramp shock is pushed outward. The aerodynamic attached surface is rather close to the boundary streamline of the secondary flow, confirming that the realization of the aerodynamic attached surface mainly depends on the mass addition effect of the secondary flow. As a result of the neglect of the tangential injection momentum, the theoretical analysis method overpredicts the influence of the air injection on the development of the momentum thickness, leading to an underprediction of the required secondary-to-primary mass flow ratio. However, this prediction error can be easily corrected, according to the integration momentum equation, if the value of u_s/u_1 is known.

The demonstration of the first ramp shock control by wind-tunnel tests shows that the shock displacement at the duct entrance increases monotonously with the increase of the secondary flow rate. The shock control capability of this technique can meet the shock control requirement of hypersonic inlets operating from Mach 4 to 6. At a secondary-to-primary mass flow ratio of 1% or less, the first ramp shock can be maintained on the cowl lip from Mach 5 to 6. Three-dimensional CFD computations are also performed according to the test conditions, and the obtained result agrees well with those of the experiments. Then, the three-dimensional effects of the air injection

process are examined, since a multihole injection plate rather than a multislot one is used. The injection process of the secondary flow embodies strong three-dimensional features, forming several sinuous flow passages between each of the two adjacent stream tubes of injected secondary flow. However, due to the buffering effect of the boundary flow, the curved ramp shock and the flow process above the boundary layer are still two-dimensional in nature, and the theoretical analysis and design method can still work.

Acknowledgment

This work was supported by National Nature Science Foundation of the People's Republic of China through grant numbers 50776044 and 90916014.

References

[1] Van Wie, D. M., "Scramjet Inlets," *Scramjet Propulsion*, edited by E. T. Curran, and S. N. B. Murthy, Vol. 189, Progress in Astronautics and Aeronautics, AIAA, Reston, VA, 2000, pp. 447–511.

[2] Takayuki, K., Nobuhiro, T., Tetsuya, S., and Masao, K., "Development Study on Axisymmetric Air Inlet for ATREX Engine," AIAA Paper 2001-1895, 2001.

[3] Watanabe, Y., Miyagi, H., and Sekido, T., "Conceptual Design Study on Combine-Cycle Engine for Hypersonic Transport," International Society for Air Breathing Engines Paper 1993-7018, Cincinnati, OH, 1993.

[4] Yusuke, M., "Multi-Row Disk Arrangement Concept for Spike of Axisymmetric Air Inlet," AIAA Paper 2004-3407, 2004.

[5] DeBonis, J. R., and Trefny, C. J., "Supersonic Wind Tunnel Tests of a Half-Axisymmetric 12°-Spike Inlet to a Rocket-Based Combined-Cycle Propulsion System," NASA TM 2001-210567, 2001.

[6] Bityurin, V. A., Klimov, A. I., Leonov, S. B., Bocharov, A. N., and Lineberry, J. T., "Assessment of a Concept of Advanced Flow/Flight Control for Hypersonic Flights in Atmosphere," AIAA Paper 1999-4820, 1999.

[7] Kopchenov, V., Vatazhin, A., and Gouskov, O., "Estimation of Possibility of Use of MHD Control in Scramjet," AIAA Paper 1999-4971, 1999.

[8] Vatazhin, A., Kopchenov, V., and Gouskov, O., "Some Estimations of Possibility to Use the MHD Control for Hypersonic Flow Deceleration," AIAA Paper 1999-4972, 1999.

[9] Kuranov, A. L., and Sheikin, E. G., "MHD Control on Hypersonic Aircraft under AJAX Concept: Possibilities of MHD Generator," AIAA Paper 2002-0490, 2002.

[10] Macheret, S. O., Shneider, M. N., and Miles, R. B., "Magnetohydrodynamic Control of Hypersonic Flows and Scramjet Inlets Using Electron Beam Ionization," *AIAA Journal*, Vol. 40, No. 1, 2002, pp. 74–81.
doi:10.2514/2.1616

[11] Shneider, M. N., Macheret, S. O., and Miles, R. B., "Analysis of Magnetohydrodynamic Control of Scramjet Inlets," *AIAA Journal*, Vol. 42, No. 11, 2004, pp. 2303–2310.
doi:10.2514/1.3998

[12] Macheret, S. O., Shneider, M. N., and Miles, R. B., "Optimum Performance of Electron Beam Driven Magnetohydrodynamic Generators for Scramjet Inlet Control," *AIAA Journal*, Vol. 45, No. 9, 2007, pp. 2157–2163.
doi:10.2514/1.16955

[13] Jagadeesh, G., Sriram, R., Hariharan, M. S., Saravanan, S., Nagashetty, K., and Reddy, K. P. J., "Experimental Investigations on the Effect of a Thermal Bump in the Hypersonic Flow Around a Flat Plate," AIAA Paper 2009-1402, 2009.

[14] Tan, H. J., Chen, Z., and Li, G. S., "A New Concept and Preliminary Study of Variable Hypersonic Inlet with Fixed Geometry Based on Shockwave Control," *Science in China. Series E, Technological Sciences*, Vol. 50, No. 5, 2007, pp. 644–657.
doi:10.1007/s11431-007-0072-7

[15] Berry, S. A., Nowak, R. J., and Horvath, T. J., "Boundary Layer Control for Hypersonic Airbreathing Vehicles," AIAA Paper 2004-2246, 2004.

[16] Lee, C. C., and Boekicker, C., "Subsonic Diffuser Design and Performance for Advanced Fighter Aircraft," AIAA Paper 1985-3073, 1985.

[17] McQuaid, J., "Incompressible Turbulent Boundary Layers with Distributed Injection," Ph.D. Thesis, Engineering Department, Cambridge University, Cambridge, England, U.K., 1966.

[18] Hirschel, E. H., *Basics of Aerothermodynamics*, Springer, New York, 2004.

[19] Tan, H. J., "Research Progress of Fluidic Hypersonic Variable Inlet," National Nature Science Foundation of China Annual Report, 2008.

[20] Sun, S., Zhang, H. Y., Cheng, K. M., and Wu, Y. Z., "The Full Flowpath Analysis of a Hypersonic Vehicle," *Chinese Journal of aeronautics*, Vol. 20, No. 5, 2007, pp. 385–393.
doi:10.1016/S1000-9361(07)60059-4

[21] Tan, H. J., and Sun, S., "Preliminary Study of Shock Train in a Curved Variable-Section Diffuser," *Journal of Propulsion and Power*, Vol. 24, No. 2, 2008, pp. 245–252.
doi:10.2514/1.31981

[22] Wang, C. P., Cheng, K. M., Wang, J. F., and Wu, Y. Z., "Flow Field Calibrations and Force Tests of an AGARD Model in a Hypersonic Wind Tunnel of NUAA," *Proceedings of the China 1st Modern Aerodynamics & Aerothermodynamics Conference*, China Aerodynamics Research Society, Beijing, PRC, 2006, pp. 356–361.

R. Bowersox
Associate Editor